Control of a Flexible Rotor AMB Compressor Test Rig with Aerodynamic Cross Coupling

Simon Mushi[a,b], Paul Allaire[a,c]

[a] Rotor Bearing Solutions International, LLC, 3277 Arbor Trace, Charlottesville, Virginia 22911, USA
[b] simon.mushi@rotorsolution.com
[c] paul.allaire@rotorsolution.com

***Abstract*—Many industrial companies are adopting magnetic bearings for high speed compressors at this time. A flexible rotor test rig of approximately 1.2 m in length was developed with four active magnetic radial bearings. It was employed to evaluate the control of destabilizing aerodynamic cross coupling stiffness Q in the center of the machine. The two end AMBs were used for support and one center AMB used to apply the cross coupled stiffness corresponding to a typical location of gas seal cross coupled stiffness sources. The fourth AMB was employed as a system exciter. Unfortunately for the compressor manufacturer and the end user, often the magnitude of the cross coupled stiffness changes with various compressor operating conditions. The test rig shaft operated up to about 18,000 rpm, through the first bending critical speed which was at approximately 14,000 rpm.**

μ-synthesis control was used to achieve highly effective control and low vibration response with the selection of an averaged value of cross coupled stiffness Q and a set of useful system uncertainty weighting functions when the controller does not have exact advance notice of the cross coupling stiffness amplitude. Details of the application of the mu synthesis controller implementation are presented. A physical approach to modeling the Q uncertainty involved selecting an expected nominal value of the real part of the first rotor system eigenvalue for the rotor first bending mode with an expected range of uncertainly above and below that value. Then suitable weighting functions were developed for the mu synthesis controller design. The measured sensitivity function was below 3 at 7,000 rpm when the rotor was subjected to high cross coupled stiffness at the center.

(a) C16 Compressor Rotor

(b) C16 Compressor

Figure 1: Solar Turbines C16 Pipeliner Compressor

I. Introduction

One of the more pressing problems in the rotating machinery industry today concerns that of high pressure compressors with gas seal/liquid aerodynamic cross coupling forces near the center of a flexible rotor [1]. Applications include compressors in the oil, gas and chemical industries. A typical compressor rotor is shown in Fig. 1a and a compressor train in Fig. 1b. An interior photograph of a multistage compressor compressor is shown in Fig. 2.

Magnetic bearings are increasingly used for the bearing system and always used in subsea applications. Often, the value of the cross coupled stiffness is not well known. Also, the seal location is near the center of the rotor but the source of damping, whether the radial bearings are fluid film or magnetic, is located at the bearings which are placed at the ends of a long flexible rotor usually operating above the first bending critical speed [2], [3]. The result of high cross coupled stiffness is the excitation of rotor whirl at the compressor first bending critical speed, as illustrated in Fig. 3. An important issue with magnetic bearing systems in such cases is the treatment of uncertainty in the magnetic bearing system.

The frequency spectrum for a compressor undergoing such instability is shown in Fig. 4. The subsynchronous vibrations (SSV) are at 2520 cpm when the operating speed is 16,000 rpm. As the compressor designs continue to evolve with higher operating speeds and pressures in magnetic bearing supported machine, the problem will require a lot of improved analysis and control technology.

The concept of a destabilizing aero cross coupled stiffness acting on a flexible rotor is illustrated by Ehrich [1] as shown in Fig. 5. The destabilizing cross coupled force F_{xc} acts in the direction of positive whirl. The pattern of poorly damped linear unstable rotor vibrations is shown in Fig. 6a where the

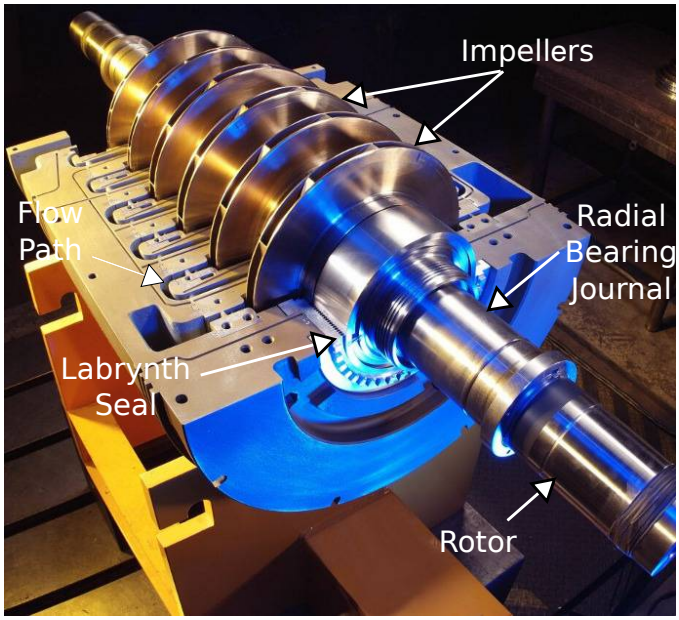

Figure 2: A multistage centrifugal compressor with upper casing removed

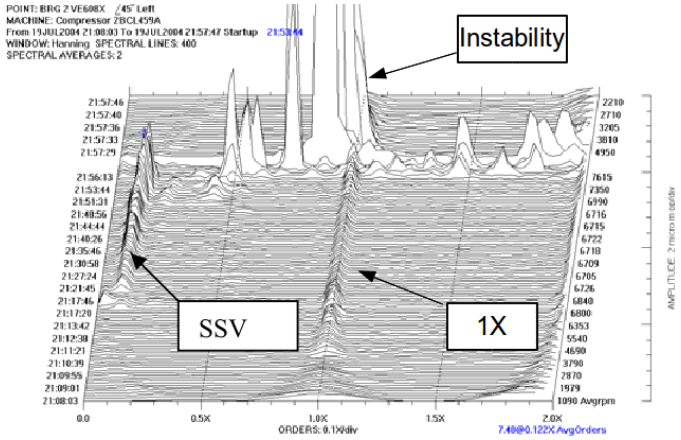

Figure 3: High Pressure Centrifugal Compressor Waterfall Plot Showing Rotordynamic Instability

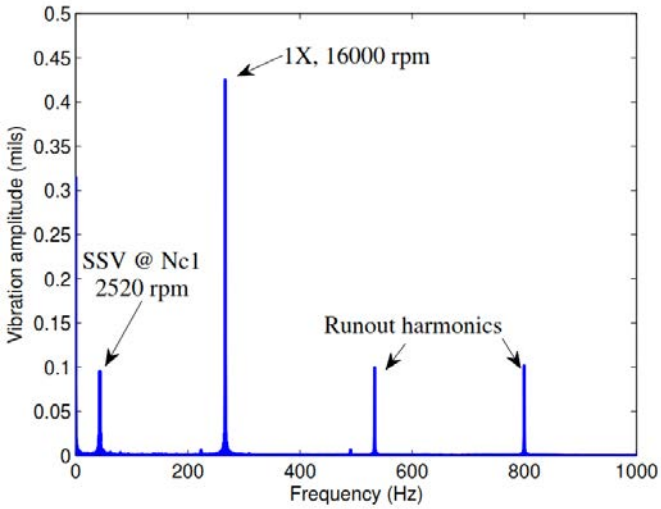

Figure 4: Spectrum Plot Showing Subsynchronous Vibration

vibrations are predicted to go off to infinity. In reality, the shaft eventually hits something, such as the auxiliary bearings and the nonlinear amplitude plot, as illustrated in Fig. 6b goes into a limit cycle. However, severe damage to the auxiliary bearings or other machine close clearance components may occur if the rotor instability is not robustly controlled.

Some formulas are used to estimate cross coupled stiffness Q such as the modified Alford equation [3] as given in Eq. (1). However, the numerical value of Q is often not well known, as noted above. This model uncertainty presents the opportunity for the application of robust modern control, which is the main subject of this paper.

$$Q = \frac{16 \times P \times MW}{D \times h \times f} \times \frac{\rho_D}{\rho_S} \tag{1}$$

The primary objective of this work is to develop a state space model of a flexible rotor-AMB system which models a compressor undergoing cross coupled excitation. The model includes uncertainty features: plant disturbances, sensor noise, actuator and system error signal [4]. A four block mixed sensitivity problem is formulated and diagonal weighting functions developed [5]. DK iteration was employed to optimize the system performance [6]. The controller was then implemented experimentally while operating well above the first bending critical speed. The system sensitivity function performance was evaluated and system damping measured using a single channel backward autoregression approach [7].

II. Flexible Rotor - AMB Test Rig with Exciters

The test rig is shown in Fig. 7. The shaft has length 1.23 m, shaft diameter 100 mm, and weight 440 N. Two disks are placed on the shaft as shown in Fig. 8. There are four magnetic bearings – two end bearings for support of the shaft, one at the center for simulation of the aero cross coupled stiffness, and the fourth one for external excitation to evaluate the system damping properties, as illustrated in Fig. 9. The direct drive motor is capable of a maximum operating speed of 18,000 rpm. A full description and characterization of the system is given in Mushi, et al. [8]. It has auxiliary bearings with radial clearance of 0.38 mm. Table I gives the details of the test rig design.

The rotor has eigenvalues (undamped natural frequencies) which change with speed due to gyroscopic forces, as illustrated in a Campbell diagram of rotor natural frequency vs. operating speed shown in Fig. 10. The red lines in Fig. 10 represent 1X and 2X times operating speed. The shaft free-free eigenvectors are shown in Fig. 11.

The plant model must be accurately determined for the control process to work as intended. The rotor characteristic transfer functions for the model nondrive end (NDEX) and drive end bearings (DEX) are shown in Fig. 12 and compared to experimental results. The agreement is good.

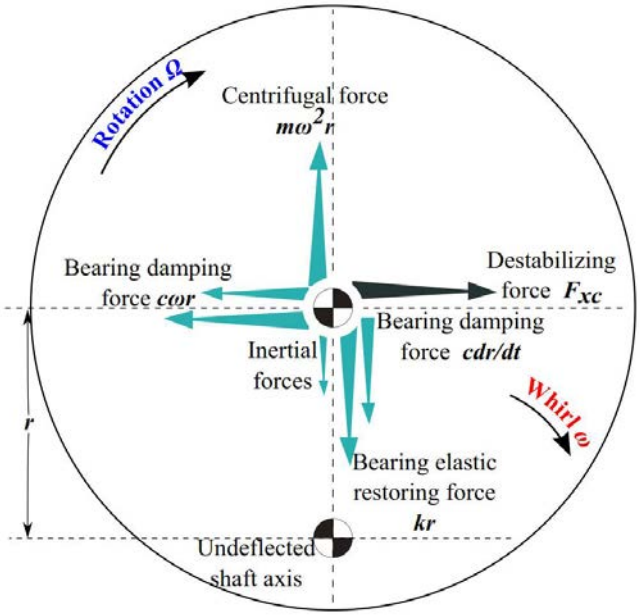

Figure 5: Cross-coupled forces

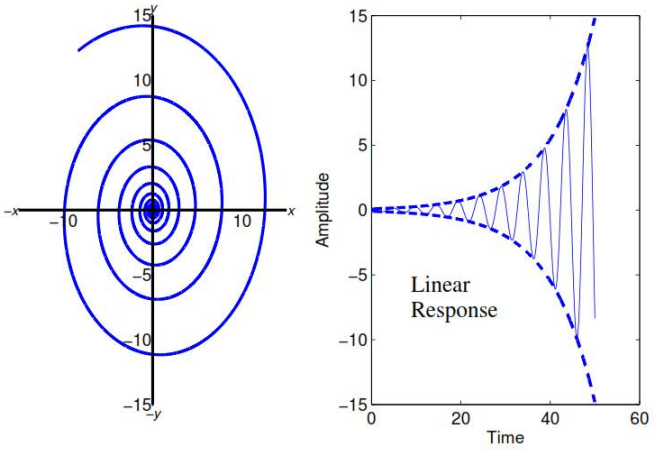

(a) Linear Response

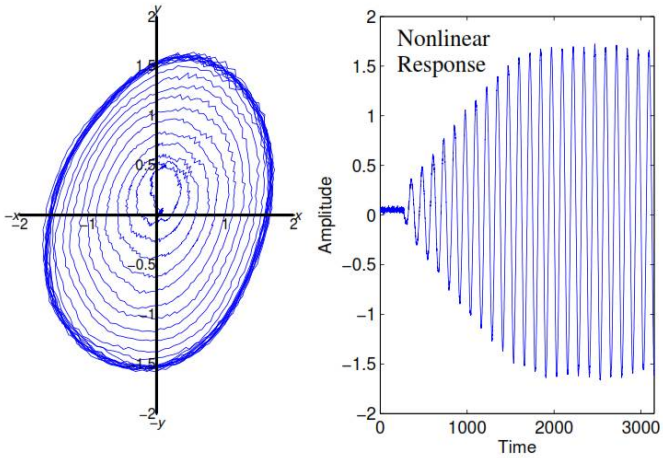

(b) Non-linear Response

Figure 6: Rotordynamic Instability Response

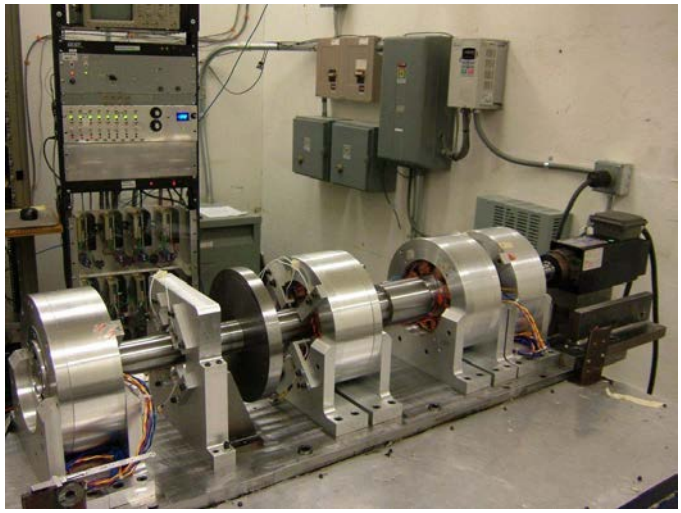

Figure 7: Active Magnetic Bearing Test Rig

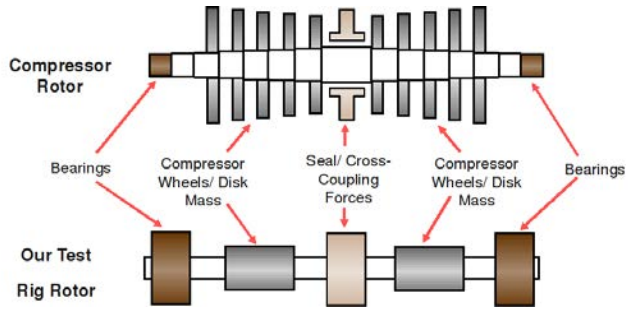

Figure 8: AMB Test Rig Approximation of a Compressor

Table I: Test Rig Properties

Property	Value	Units
Total rotor weight	440	N
Rotor length	1068	mm
Bearing span	918	mm
Average shaft diameter	57.7	mm
Area moment of inertia	5.43×10^{-7}	m^4
Mass moment of inertia	0.0880	$kg{\cdot}m^2$
1st free-free lateral bending mode	13,200	rpm
Maximum speed	18,000	rpm
Motor power	3.7	kW
AMB radial clearance (average)	550	μm
Backup bearing clearance	250	μm
Support AMB stator length	43.6	mm
Support AMB bias current	4.0	A
Support AMB negative stiffness	0.6 - 0.9	MN/m
Support AMB current gain	90-100	N/A
Power amplifier DC bus	150	V
Controller sampling rate	12	kHz

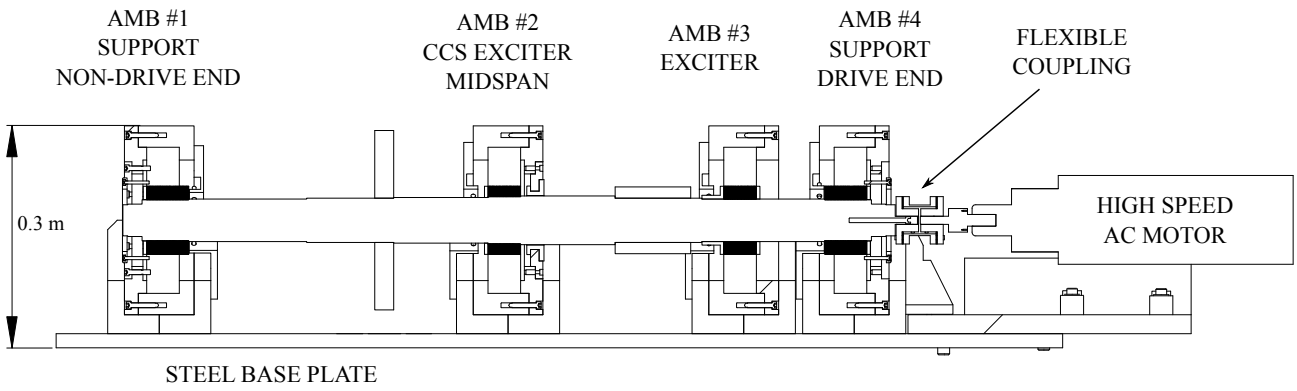

Figure 9: AMB Test Rig Elevation View

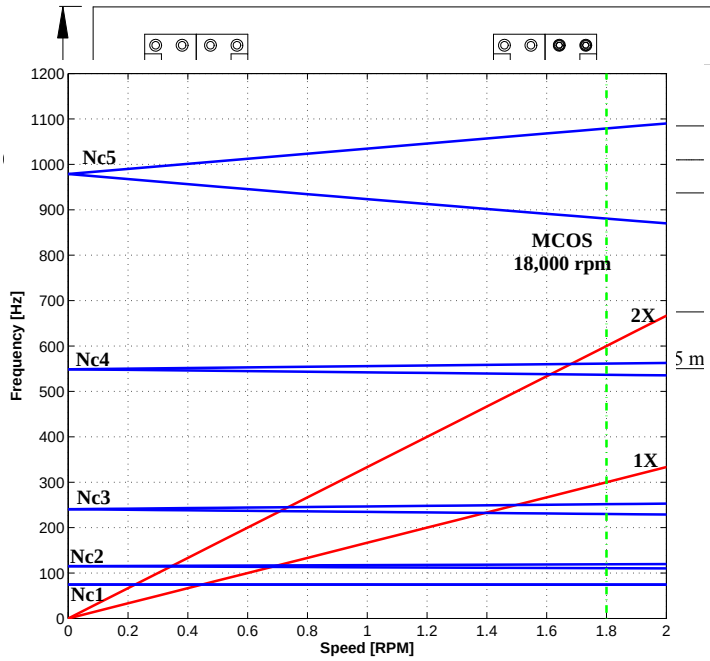

Figure 10: Rotor Campbell Diagram

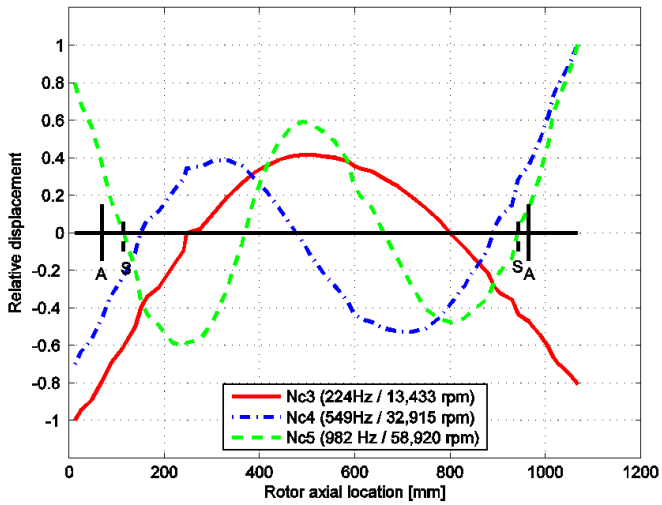

Figure 11: Rotor Undamped Mode Shapes

III. A CONTROL SYSTEMS PERSPECTIVE: MODEL BASED SYNTHESIS AND ANALYSIS TOOLS

A. *Mu-synthesis and analysis*

The μ-synthesis technique is the only multivariable control design approach that directly addresses the robust performance problem, i.e., the design of a stabilizing control law that guarantees a performance specification for all plant model perturbations within a defined set [9]. The theory was introduced in the 1980s, and steadily improving commercial software tools have been available in the last decade. A few notable prototype industrial rotor-AMB systems utilizing μ-synthesis have been documented in open literature [10], [11], but there is scant evidence the application of μ-analysis techniques. These facts highlight the significant challenges which remain to be addressed in order for the full potential of these modern techniques to be realized.

The most prominent challenge is the relatively high design complexity involved with these techniques and concerns regarding practical implementation and field troubleshooting. A state space block diagram of the flexible rotor-AMB plant for this test rig is shown in Fig. 13.

The last issue, field troubleshooting, is helped by the advent of remote diagnostic and communications capabilities of current AMB control systems that allow online system identification and auto-tuning [12], [13]. The second concern is less of an issue nowadays as the available computing power for executing real-time control algorithms continues to increase.

The first issue mentioned looms large as the translation of engineering performance specifications into formal constraints in the form of weighting functions, uncertainty models, and other design criteria remain a largely heuristic process [14]. These issues are not unique to μ-techniques, but symptomatic of the limited penetration of advanced multivariable control into industrial systems. One may argue why bother with an investment in μ-synthesis if a hand-tuned compensator designed by a control practitioner has the potential to deliver similar performance (this is particularly relevant in the industrial control system community dominated by hand tuned PID-like compensators). Maslen and Sawicki [15] answer this question

by suggesting that investments in μ-techniques result in an improvement in the engineering process. The complexity and performance demanded of modern precision control systems is such that the notion when provided with a model and performance specification one can "turn a crank" and deliver a control law is naive [16]. Assuming that an accurate nominal plant model is available (a nontrivial task in many cases [17]), the remaining challenge is the development and continuous refinement of performance specifications and uncertainty models that yield controllers approaching the theoretical maximum achievable performance.

B. Mixed sensitivity weighting function selection

Performance specifications are characterized in the frequency domain as typical rotor-AMB systems lack specific time domain specifications, e.g., overshoot and settling time and these do not fit directly into the frequency based robust H_∞ and μ-synthesis frameworks [14]. The loop-shaping approach is preferred over the signal based approach as it does not require implementation specific information on the magnitudes of signals in the closed-loop system [18]. Sensitivity functions serve as useful measures of control performance in the frequency domain. Considering a unity feedback connection of a plant $G(s)$, controller $K(s)$, with exogenous disturbance forces acting on the plant input and output d_i and d_o respectively, sensor noise n and control effort u, controlled variable output y and controller reference input signal r. A block diagram of the flexible rotor AMB system is given in Fig. 14.

$$y(s) = T_i(s)r(s) + S_o(s)d_o(s) + GS_o(s)d_i(s) - T_o(s)n(s), \quad (2)$$

$$u(s) = KS_o(s)r(s) - LS_o(s)d_o(s) - S_i(s)d_i(s) - KS_o(s)n(s) \quad (3)$$

where several sensitivity functions can be defined [19]:

- Input Sensitivity $S_i(s) \triangleq (I + K(s)G(s)) - 1$: a measure of system rejection of disturbances at plant inputs;
- Complementary Input Sensitivity $Ti(s) \triangleq K(s)S_o(s)G(s)$: a measure of the effect of disturbance at the reference input on the control signal;
- Output Sensitivity $S_o(s) \triangleq (I + G(s)K(s)) - 1$: a measure of the noise rejection and closed-loop command tracking;
- Complementary Output Sensitivity $T_o(s) \triangleq GS_i(s)K(s)$: a measure of the effect of noise on the control signal;
- Process Sensitivity $GS_i(s)$: a measure of the closed loop mechanical compliance (reciprocal of stiffness) of the rotor-bearing;
- Control Sensitivity $KS_o(s)$: a measure of the control effort.

The ISO/API input sensitivity function limit for class A (new machines) is less than 3.0. An output sensitivity function for the test rig NDEX and DEX sensors with collocated PID control is given in Fig. 15. It exceeds the class A limit.

A bound on a single sensitivity function, such as the output sensitivity takes the form of $||W_s(s)S(s)||_\infty < 1$, where $W_s(s)$ is a stable, proper transfer function. If the inequality is satisfied, the inverse weighting function $W_s^{-1}(s)$ represents the upper bound on $S(s)$. A typical inverse weighting function to achieve low frequency disturbance attenuation, for example, is shown in Fig. 16.

For high performance motion control systems typified by rotor-AMB applications, a single sensitivity provides insufficient degrees of freedom to simultaneously specify disturbance rejection region while minimizing controller bandwidth and as well as reference tracking performance [4]. By combining several weighted sensitivity functions, i.e., $||W_s(s)S(s)||_\infty < 1$, $||W_u(s)KS(s)||_\infty < 1$, and $||W_r(s)T(s)||_\infty < 1$, into a stacked objective:

$$\min_K \left\| \begin{array}{c} W_s(s)S(s) \\ W_u(s)KS(s) \\ W_r(s)T(s) \end{array} \right\|_\infty < \gamma \quad (4)$$

and letting the $H\infty$ synthesis process handle the trade-offs between competing goals so that maximum performance may be attained.

Experimental measurements of the sensitivity function for the x and y axes with cross coupled stiffness applied at the center AMB with standard PID control are presented here. The first one is given in Fig. 17 for a cross coupled stiffness value of 2.6MN/m and a peak sensitivity function of 2.5. With this level of cross coupling, the rotor satisfies the criteria of class A operation. With a higher value of cross coupled stiffness of 3.15 MN/m, the peak sensitivity function shown in Fig. 18 is 4.6 MN/m. Now the rotor does not qualify as a class A operation.

The four-block problem in Eq. (4) provides a means for any three non-complimentary functions to be weighted individually. A diagram of the four block system is shown in Fig. 18. The advantages of the four-block scheme over the two or three block problems are its well-posedness and avoidance of pole-zero cancellation by the synthesized controller [20], [21].

Figure 19 illustrates the feedback connection of the weighting functions to the plant and controller blocks. The reference input r and disturbance input d are new signals introduced. Shaping the control sensitivity function $KS(s)$ is necessary to effect a controller gain roll-off at high frequencies to avoid exciting unmodeled dynamics or amplifying sensor noise. Shaping the process sensitivity function $GS(s)$ affects the closed-loop damping, while the shaping the output sensitivity $S(s)$ translates directly to modifying the disturbance rejection properties. The complimentary sensitivity $T(s)$ cannot be shaped independently of the aforementioned functions as a result of the complimentary nature of the four sensitivity functions.

The system gain from disturbance inputs to performance outputs is

$$\left[\begin{array}{c} z_1 \\ z_2 \end{array} \right] = T_{zw} \left[\begin{array}{c} d \\ r \end{array} \right] \quad (5)$$

and to guarantee the desired nominal performance specified by the above sensitivity functions, the cost γ to be minimized by the controller K must be less than unity.

This results in upper bounds on **S**, **GS**, **KS** and **T**, are $\left(\mathbf{W_p W_r}\right)^{-1}$, $\left(\mathbf{W}_p\mathbf{W}_d\right)^{-1}$, $\left(\mathbf{W}_u\mathbf{W}_r\right)^{-1}$, and $\left(\mathbf{W}_u\mathbf{W}_d\right)^{-1}$, respectively. The cost function represented by Eq. (6) solves the

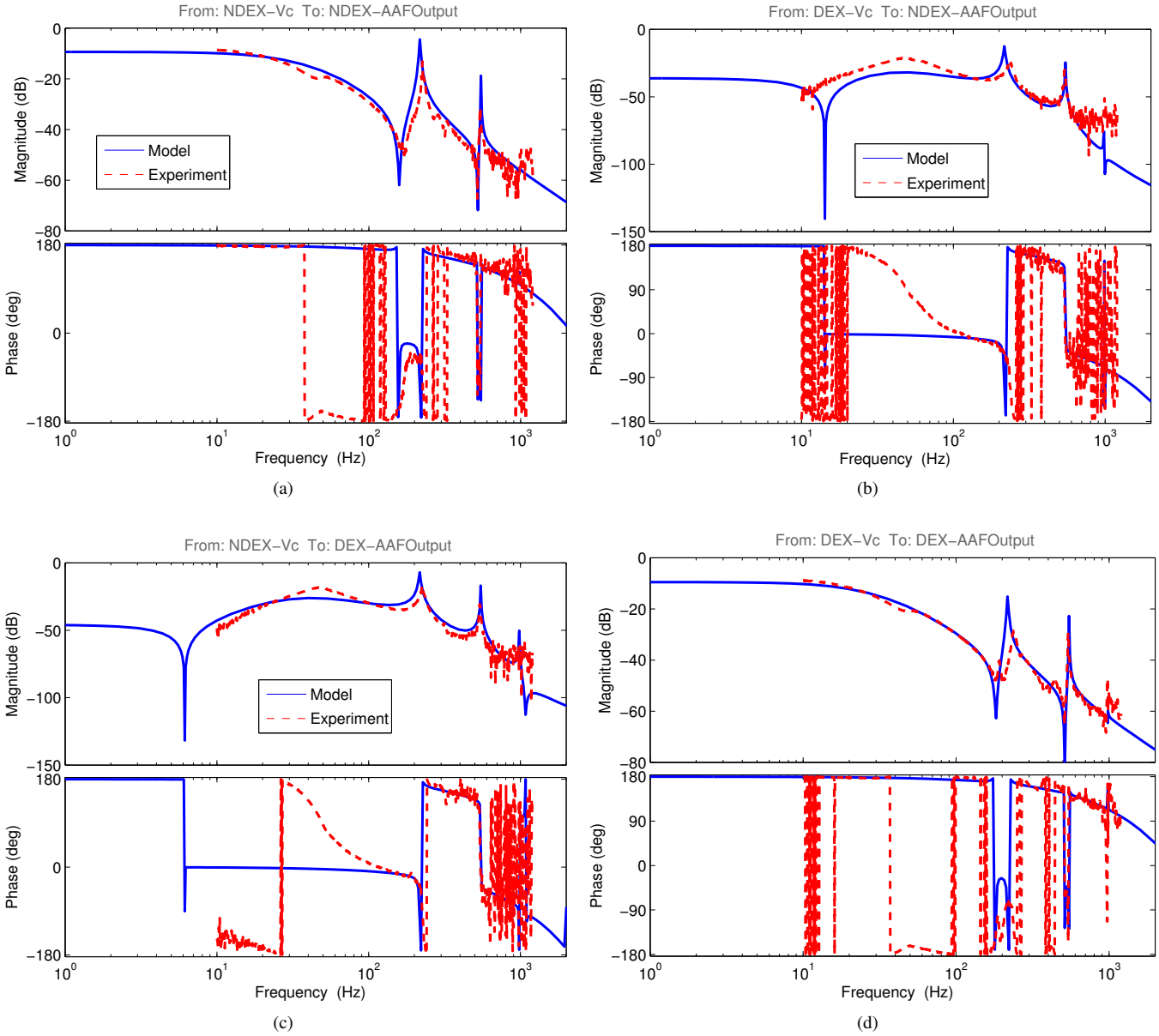

Figure 12: Rotor Transfer Functions

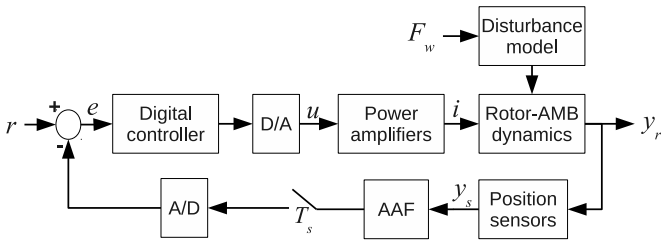

Figure 13: Control System Block Diagram

nominal performance problem. Since Δ has been defined in block diagonal form, the straightforward extension of Eq. (6) to solve the robust performance problem is carried out by defining the structured uncertainty set Δ and finding the controller that minimizes $\mu_\Delta(\mathbf{M})$ using D-K iteration [22].

$$\begin{aligned} \min_K \left\| T_{zw} \right\|_\infty &< \gamma \\ \left\| \begin{bmatrix} \mathbf{W}_p(\mathbf{I}+\mathbf{GK})^{-1}\mathbf{W}_r & \mathbf{W}_p\mathbf{G}(\mathbf{I}+\mathbf{GK})^{-1}\mathbf{W}_d \\ \mathbf{W}_u\mathbf{K}(\mathbf{I}+\mathbf{GK})^{-1}\mathbf{W}_r & \mathbf{W}_u\mathbf{GK}(\mathbf{I}+\mathbf{GK})^{-1}\mathbf{W}_d \end{bmatrix} \right\|_\infty &< \gamma \\ \left\| \begin{bmatrix} \mathbf{W}_p\mathbf{S}\mathbf{W}_r & \mathbf{W}_p\mathbf{G}\mathbf{S}\mathbf{W}_d \\ \mathbf{W}_u\mathbf{K}\mathbf{S}\mathbf{W}_r & \mathbf{W}_u\mathbf{T}\mathbf{W}_d \end{bmatrix} \right\|_\infty &< \gamma \end{aligned} \tag{6}$$

IV. Modeling Uncertainty

Modeling of the impact of the cross coupled stiffness (CCS) or Q on the open-loop plant dynamics can be carried out directly from first principles or phenomenologically. In the case of the former, an uncertain CCS is modeled directly

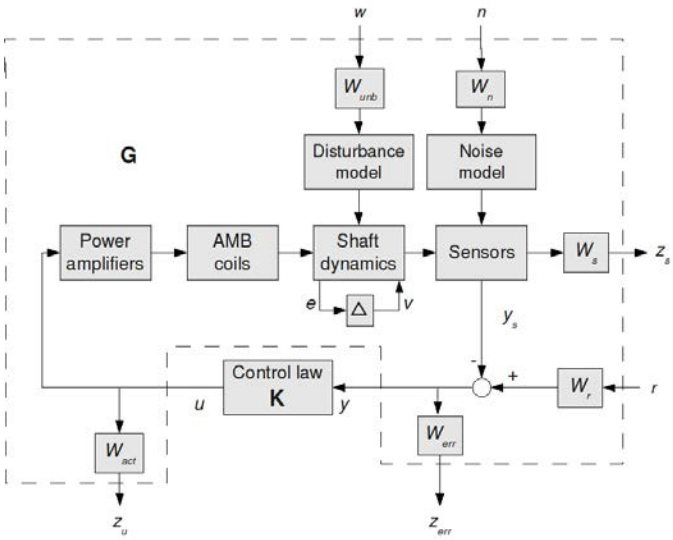

Figure 14: AMB System Block Diagram

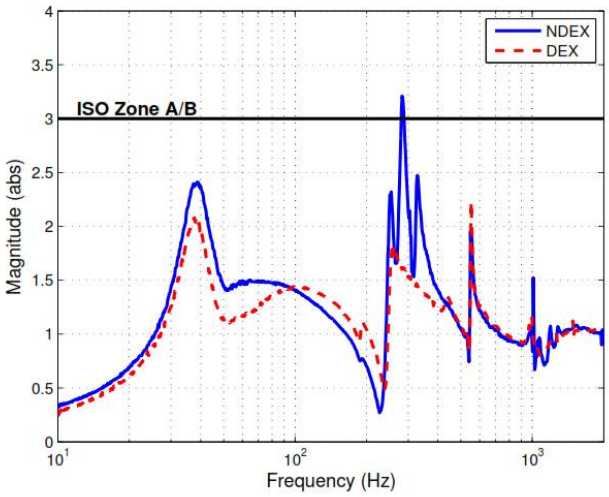

Figure 15: Output sensitivity of NDEX and DEX channels of collocated PID controller.

as a real-valued stiffness varying between 0 and 4 MN/m acting at the rotor midspan. Therefore, the associated rotor displacements as shown in Eq. (7) are the shaft finite element locations x_{23} and y_{23}. The system schematic is shown in Fig. 8.

$$\mathbf{M}\ddot{\mathbf{q}} + (\mathbf{D} + \Omega\mathbf{G})\dot{\mathbf{q}} + \mathbf{K}_s\mathbf{q} = \mathbf{B}_{\text{mag}}\mathbf{F}_{\text{mag}} + \mathbf{B}_w\mathbf{F}_w \quad (7)$$

$$\mathbf{y}_r = \mathbf{C}\mathbf{q} \quad (8)$$

Assuming the CCS (Q) is the sole exogenous disturbance in the system:

$$\mathbf{B}_w\mathbf{F}_w = Q \begin{bmatrix} 0 & 1 \\ -1 & 0 \end{bmatrix} \begin{Bmatrix} q_{x_{23}} \\ q_{y_{23}} \end{Bmatrix} \quad (9)$$

where the stiffness Q can be modeled in two ways:

1) As a real parameter varying from 0 to 1.8 MN/m with a nominal value of 0.9 MN/m denoted CCS Model 1, or

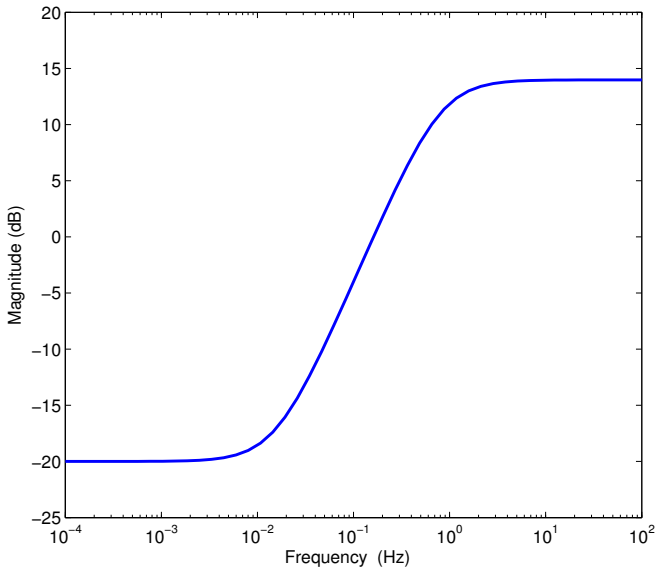

Figure 16: Typical inverse performance weighting function $W_p^{-1}(s)$

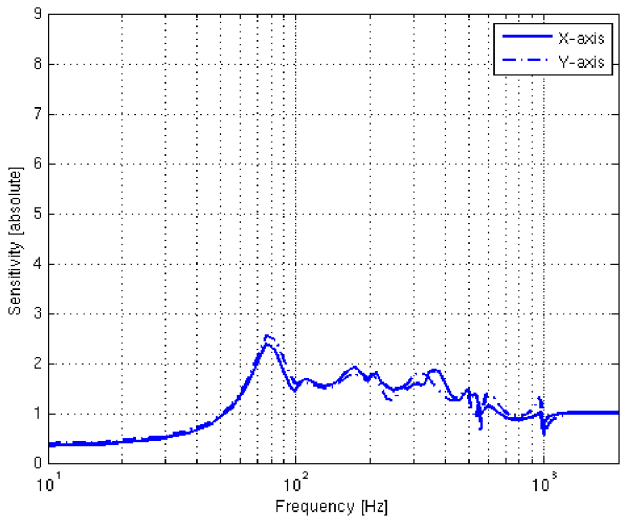

Figure 17: Sensitivity Function, Q = 2.6 MN/m

2) As a real parameter varying from 0 to 2.4 MN/m with a nominal value of 1.2 MN/m denoted CCS Model 2.

The resulting model shows, as expected, increased coupling between the x and y lateral rotor displacements at all rotating speeds. Figure 20 demonstrates the coupling with four Bode plots and a singular value plot of the nominal plant augmented with the uncertainty defined by CCS Model 1.

While the demonstrated coupling between the axes is mathematically correct, the additional dynamics complicate the model and present an open-loop plant that is more of a challenge to validate and control. Increased conservatism arises as Q affects several parameters within the plant model. While the effect on the Nc1 rotor pole is important and the most desired to be captured by this uncertainty definition,

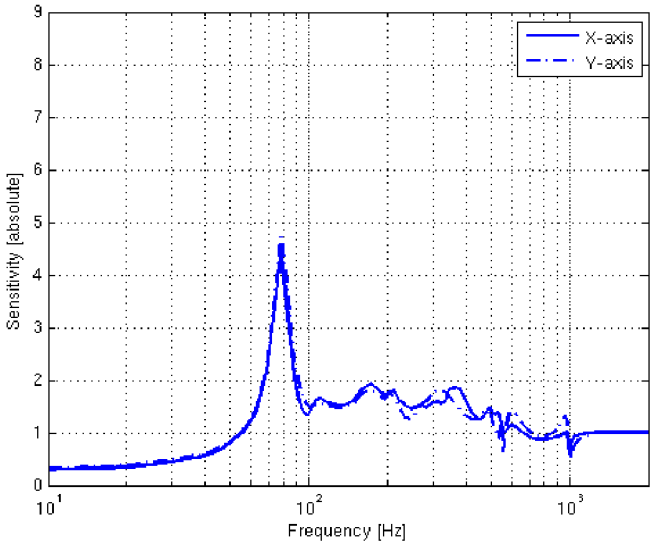

Figure 18: Sensitivity Function, Q = 3.15 MN/m

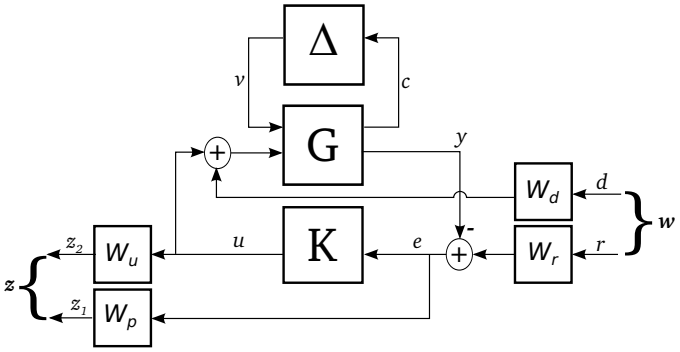

Figure 19: Interconnection of performance weights with plant, uncertainty description and controller

several collateral effects occur such as the perturbation of Nc3 and Nc4 poles and zeros are not desired.

Phenomenological modeling of the uncertainty attempts to model the empirical effect of the CCS on the plant rather than the intrinsic dynamics of the rotor-AMB system which have been shown to be highly conservative [22]. By far the most significant effect of CCS on the plant is the trajectory of the RHP pole of Nc1 as CCS is varied (see Fig. 21 and Table II). Increasing the CCS has the effect of splitting the real RHP pole due to Nc1 into a complex pole that moves further to the right of the complex plane. Assuming the Nc1 complex eigenvalue (an RHP pole) of the form $\sigma \pm j\omega$, the effect of CCS on σ can be modeled either:

1) as a real-valued uncertainty varying from 200 to 240 rad/s with a nominal value of 220 rad/s denoted CCS Model 3, or
2) as a real-valued uncertainty varying from 200 to 260 rad/s with a nominal value of 230 rad/s denoted CCS Model 4.

An eigenvalue perturbation description was used to represent the variations above, and combine into the state-space description of the rotor-AMB system. The advantages of

Table II: The effect of varying CCS magnitude on the location of Nc1 eigenvalue

Q, N/m	Eigenvalue	f_n, Hz	ζ
0	195	31	-1
$5 \cdot 10^5$	$199 \pm 55.7j$	32.9	-0.963
$1 \cdot 10^6$	$199 \pm 55.7j$	32.9	-0.963
$1.5 \cdot 10^6$	$207 \pm 80.7j$	35.5	-0.928
$2 \cdot 10^6$	$217 \pm 104j$	38.2	-0.904
$2.5 \cdot 10^6$	$227 \pm 125j$	39.8	-0.908
$3 \cdot 10^6$	$237 \pm 104j$	44.1	-0.855
$4 \cdot 10^6$	$256 \pm 104j$	44.9	-0.818

the phenomenological approach are that x,y coupling (off-diagonal gain) is minimized, allowing the nominal model developed. Effects of the uncertain CCS modeled through a single eigenvalue perturbation remain largely in the low frequency band around Nc1. The uncertainty set described by CCS Model 3 and 4 is thus compact for the equivalent physical responses. The gap metrics of CCS Model 3 and CCS Model 4 are identically 0.624 indicating a not unreasonable distance from the nominal plant description.

V. Controller Evaluation

The optimum benchmark controller was developed after several iterations of the weighting function modification and control synthesis. Details of the optimization process are given in Mushi [22]. The benchmark serves as the root from which other controllers were developed. Key properties of the benchmark controller are evaluated below to highlight the details of its construction. The analysis largely focuses on the control response, and the Bode plots and the singular value plots are used to show the magnitude and phase, MIMO response, and closed-loop actuator stiffness of the controller.

Convergence of the DK iteration of the μ-upper bound occurred within 4 iterations. A zeroth order D-scaling matrix was generated during each iteration. This results in the minimum achievable controller order of 48. A discrete-time implementation of this control law sampled at 12 kHz executes within 52 us on the DSP hardware. This represents 62% of the available interrupt [23]. The evolution of the μ-upper bound as a function of frequency during the D-K iterations and the minimum peak value of μ is 1.02.

Analyzing the pole and zero locations of the controller is important to examine whether pole-zero cancellation has occurred between the controller and plant. Pole-zero cancellation is at best highly undesirable due to the absence of robust stabilization, and at worst likely to produce unstable controllers if the plant has RHP zeros. The poles and zeros of the benchmark controller are shown in Fig. **??**, where it is confirmed no cancellation with plant poles or zeros occurs. This is a byproduct of using the four-block mixed sensitivity framework for specifying the controller performance. Interestingly, the controller contained four pairs of complex RHP zeros at $205 \pm 3449j$, $189 \pm 3431j$, $81 \pm 1180j$, and $80 \pm 1175j$. These non minimum-phase zeros introduce phase lag in the vicinity of the bending modes and serve to augment their damping [24].

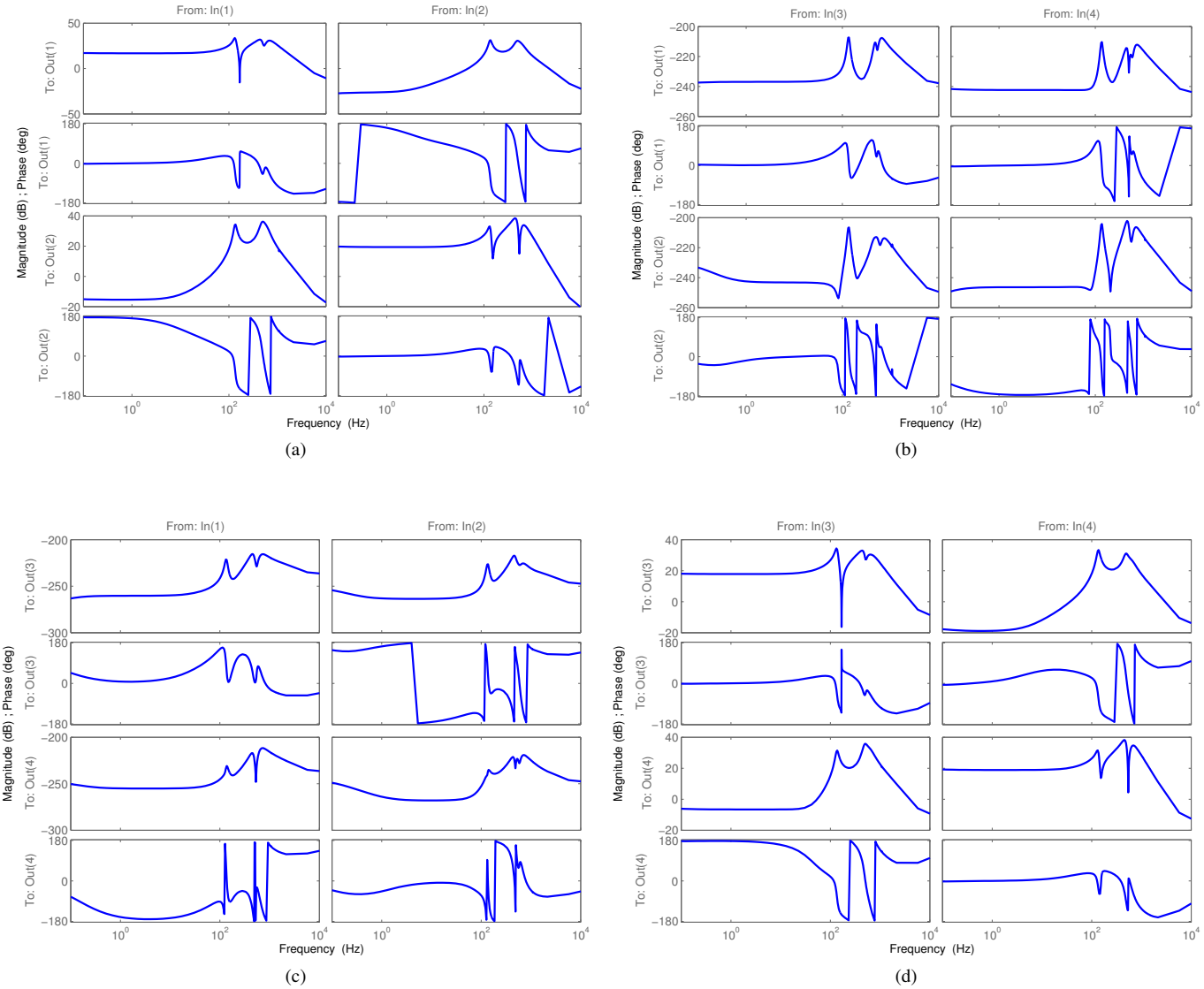

Figure 20: Bode plots of response of Benchmark I controller across all four channels. In and Out refer to input and output directions, while the indices 1, 2, 3 and 4 refer to NDE-X, DE-X, NDE_Y and DE-Y, respectively.

The equivalent closed-loop mechanical stiffness of AMB actuator as a function of frequency [25] is:

$$K_{eq_{ij}}(j\omega) = K_i G_s G_{as} \mathrm{Re}\big(K_{ij}(j\omega)\big) \tag{10}$$

where $\mathbf{G}_s$ is the sensor gain, $\mathbf{G}_{as}$ is the amplifier gain, K_i is the AMB current gain and $K_{ij}(j\omega)$ is the frequency response of the i, j controller channel. This equivalent stiffness is plotted in Fig. 22 can be compared to similar plots for mechanical bearings. The plots show that a similar stiffness is apparent along the x and y axes of each bearing, while the driven-end bearing has an overall higher low-frequency stiffness than the non driven-end bearing.

VI. μ-Analysis of Controllers with Cross-Coupled Stiffness Uncertainty

The aim of this section is to examine the changes introduced by the addition of a cross coupled stiffness Q uncertainty description to a plant model already augmented with gyroscopic model uncertainty. Several different models with CCS uncertainties – CCS models 1, 2, 3, and 4 – are considered in this section.

The two controllers synthesized with block-diagonal performance weight $W_{p,4}$ and either CCS Model 3 or CCS Model 4 yielded a smaller increase in μ from the Benchmark cases as compared to the controller designed with 70% support Figs. 23, 24, the RS bounds have a sharp peak close to 200 Hz seen with CCS Model 3. Breaking down the nominal performance of these two controllers again reveals similar system gain behavior with frequency to Benchmark Ic3 [22]. A lower bias current was necessary for block diagonal $\mathbf{W}_{p,4}$ Ic2 controller to achieve stable suspension of the rotor. This is likely to contribute to slightly reduced performance with respect to CCS since a higher bias current is associated with

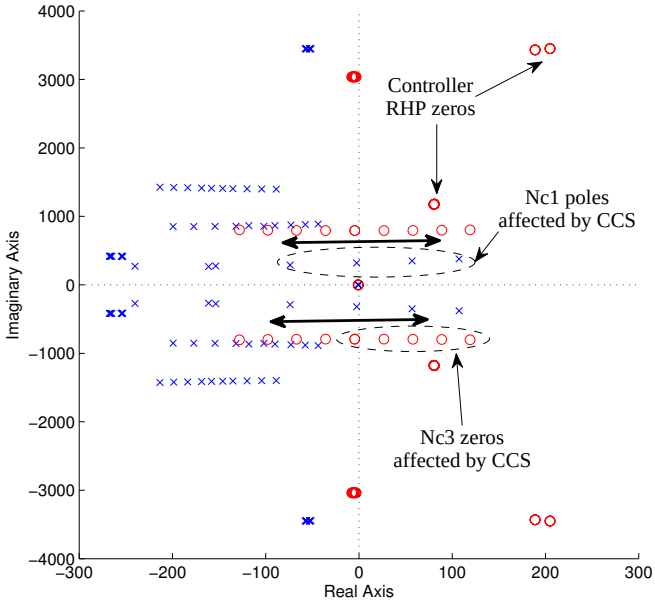

Figure 21: Pole-zero trajectory of closed loop rotor-AMB system at 0 rpm with CCS(0 to 2400 N/mm)

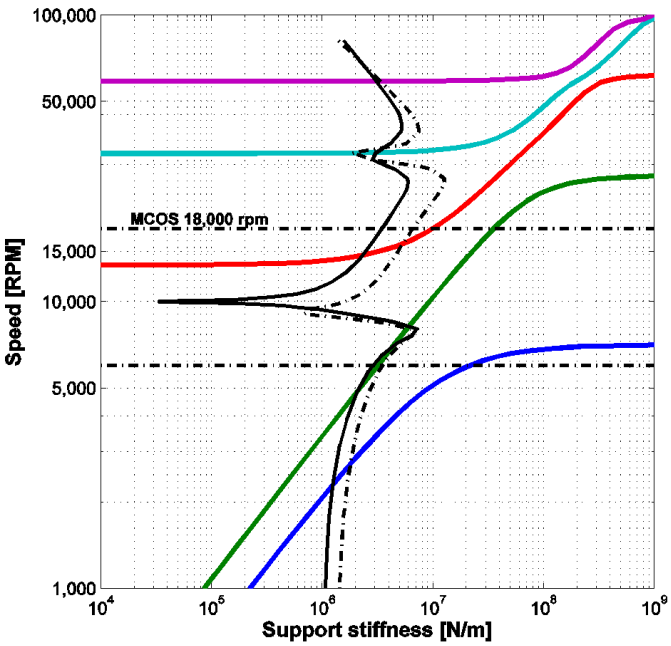

Figure 22: Undamped critical speed map showing eigenvalues as a function of support stiffness. The closed-loop actuator stiffness for an exemplary controller is overlaid.

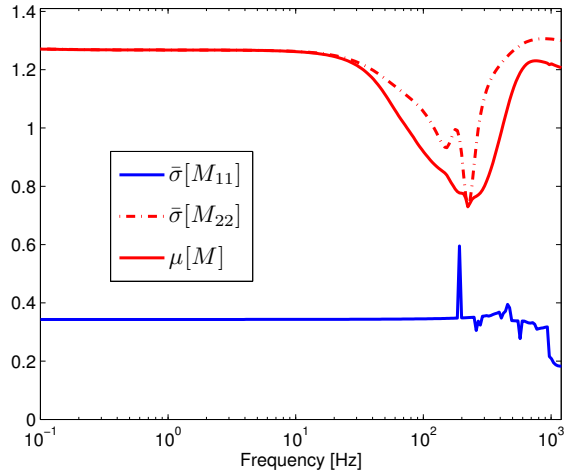

(a) NS, NP, RP bounds.

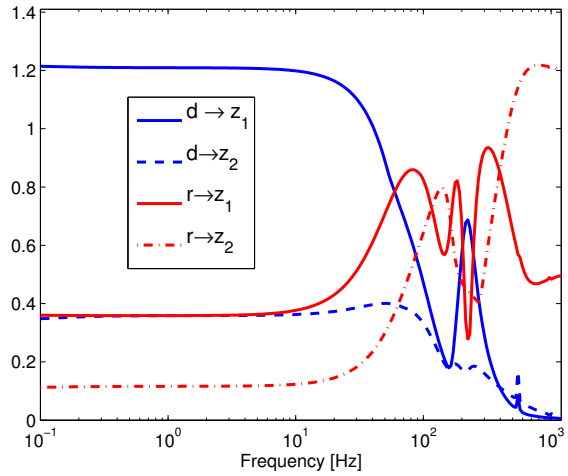

(b) Nominal performance breakdown

Figure 23: μ-Analysis of nondiagonal performance weight $W_{p,4}$ controller designed with plant uncertainty including *Speed Model 2* and *CCS Model* 3.

higher values of the AMB current gain K_i.

VII. Experimental Results

The benchmark controller was tested in the flexible rotor-AMB test rig. Bode plots and phase angles for 8 of the 16 total loop transfer functions taken at 0 rpm are shown in Fig. 25.

The measured output sensitivity functions measured at 5,000 rpm and 10,000 rpm are shown Bode plots in Fig. 26. The measured amplitude values for the inverse weighting function performance bound is less than the ISO/API class A/B limit indicating high levels of disturbance rejection. The peaks values occur in the range of the rigid body modes suggesting a variation of the actuator gain properties K_i, K_x, from their expected values. There are no peaks near bending modes which is desired for robust performance. The peak sensitivity was measured to be 9.17 dB (2.87) over all of the control channels. Other sensitivity functions were also measured with

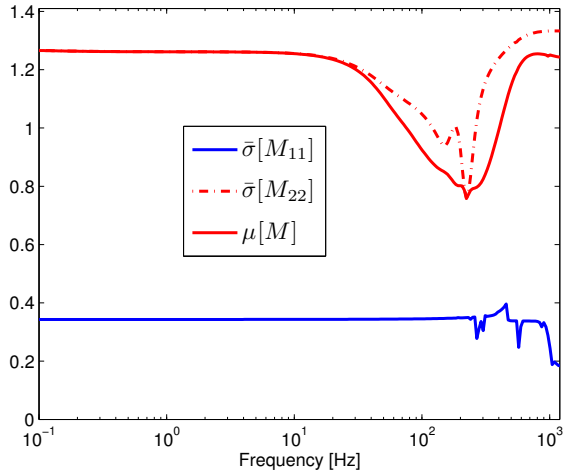

(a) NS, NP, RP bounds.

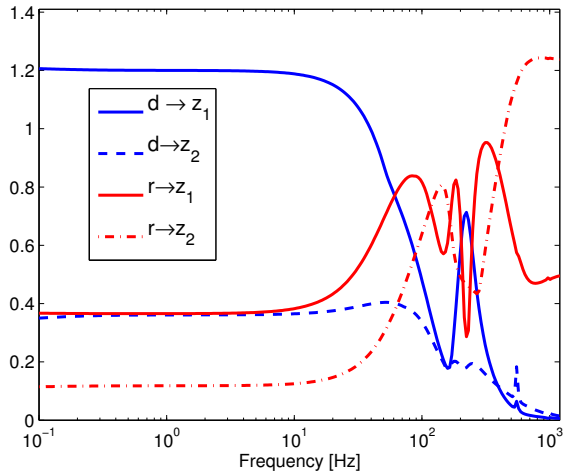

(b) Nominal performance breakdown

Figure 24: μ-Analysis of nondiagonal performance weight $W_{p,4}$ controller designed with plant uncertainty including *Speed Model 2* and *CCS Model 4*.

similar robust results. The complementary sensitivity function results for sensor noise are shown in Fig. 27.

VIII. Forced Response

The rotor was able to operate above the first critical speed, at approximately 14,000 rpm as shown in Fig. 28. A high speed balancing run was required to get through the first critical speed and operate up to 18,000 rpm.

IX. Cross Coupled Stiffness Stability Threshold

The cross coupled stiffness Q destabilizing forces were applied to the rotor using the center AMB actuator. The rotor rigid body modes are easily stabilized [26]. The stability of the first rotor bending mode Nc1 is strongly affected by the cross coupled stiffness. The maximum value of the cross coupled stiffness Q prior to the onset of instability is denoted as the stability threshold. An equivalent statement is that when the system effective damping is zero, the linear stability threshold has been reached. The cross coupled stiffness reduces the damping of the forward whirl mode until it reaches instability.

The two best system models of cross coupled stiffness Q effects assumed that the complex eigenvalue of the excited first rotor bending mode had certain characteristics. In the first Q controller model, labeled No. 3, a real valued uncertainty of the first bending mode eigenvalue from 200 rad/sec to 240 rad/sec was modeled with the nominal value of 220 rad/sec. In the second Q controller, labeled No. 4, a real valued uncertainty of the first bending mode eigenvalue from 200 rad/sec to 260 rad/sec was modeled with the nominal value of 230 rad/sec. This specification of uncertainty is a physical approach to the Q stiffness effects.

To experimentally determine the stability threshold, successively higher cross coupled stiffness values were imposed on the rotor. The system damping ratio was measured by using a blocking approach [27]. Circular rotor excitation was applied using the quarter span AMB an the response measured, as shown in Fig. 29.

Values of Q used in the testing were Q = 0, 600, 1200, 1800 N/mm operating at 7,000 rpm. The experimental stability plots of system log decrement vs. Q are given in Fig. 30. The first measurement is without the Q uncertainty model, as shown in Fig. 30a for several benchmark controllers. The second measurement is with the Q uncertainty model, as shown in Fig. 30b. The Q controller model 3 with block diagonal weighting matrices performed the best in Fig. 30b.

X. Conclusions

The issue of robust control related to destabilizing seal aero cross coupled stiffness in high pressure industrial compressors using AMB supports does not have a simple solution. However, the research reported in this paper shows that modern control with the mu synthesis approach provides one suitable method of solution. Usually these compressors are operated supercritical and with the issue of subsynchronous vibration a problem. While a few prototype industrial machines with μ-synthesis control have been reported in the literature, there has not been very much literature reporting on the problem of cross coupled stiffness with the level of detail found in this paper.

A systematic treatment of mu synthesis modeling and analysis has been presented to illustrate the modeling procedure. An extensive treatment of system uncertainties, plant input disturbances, plant output disturbances, sensor noise, control effort and controller input reference signal, has been presented with a four block uncertainty model. A total of 14 controllers were investigated with the focus here on two of the most successful ones. It has been shown that when an accurate model of the flexible rotor-AMB system including all important features – rotor, AMB, sensors, amplifiers, gyroscopic effects, cross coupled stiffness estimates – and the uncertainty models with suitable weighting functions, the controller is successful in achieving robust control. DK iteration optimization has been shown to achieve the desired mu control level in only a few iterations.

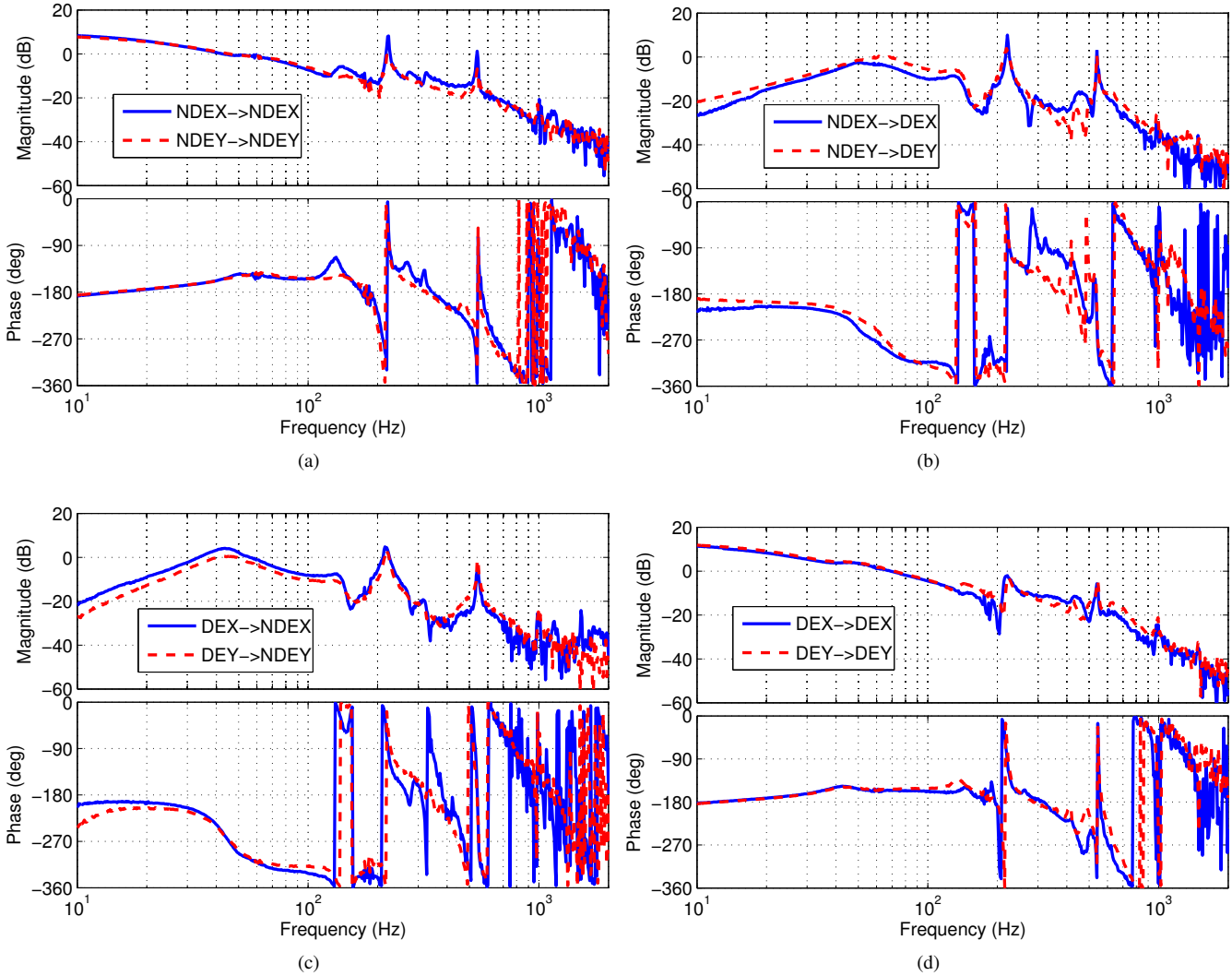

Figure 25: Bode plots of measured loop transfer functions.

The method of assessing the system performance through sensitivity functions was an approach jointly adopted relatively recently by ISO/API and employed in this work. The experimental results show that the best controllers developed in this research were able to qualify the test rig performance as ISO/API class A even with high levels of aero cross coupling. This result has not been reported in the literature prior to this paper.

Both of the best Q controllers were successful in stabilizing the first rotor bending mode using a physical approach. This approach shows that the key to controlling aero cross coupled stiffness due to seals at the center of an industrial compressor is treating the real part of the Nc1 eigenvalue with a nominal value of expected cross coupled stiffness and a range of values treated as uncertainty in the rotor AMB system. A suitable uncertainty weighting function structure must be included to properly stabilize the system.

There were also some unexpected results. For example, the controllers with the block diagonal cross coupled stiffness uncertainty performance weighting did well in providing robust control of the system for the stability threshold. However, another controller without that performance weighting function provided a stability threshold that was as good and slightly better.

It seems likely that the methods developed in this paper have a useful purpose in industrial high pressure compressor with AMB supports. It is hoped that this paper assists in that effort.

Authors' Note

The authors would like to thank the organizers of the ISMB 14 Symposium for allowing such a long keynote paper. While this paper provides a lot of detail regarding this research topic, it is noted here that many aspects of this research project could not be included in this paper even with all of the material which was included. The authors recommend readers who want to know more to consult Mushi [22].

REFERENCES

[1] F. F. Ehrich, *Handbook of Rotordynamics*. Krieger Publishing Company, 2004.

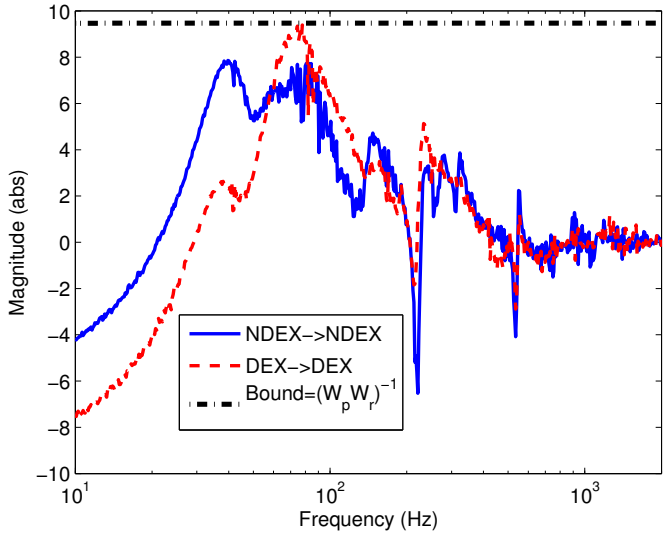

(a) 5,000 rpm

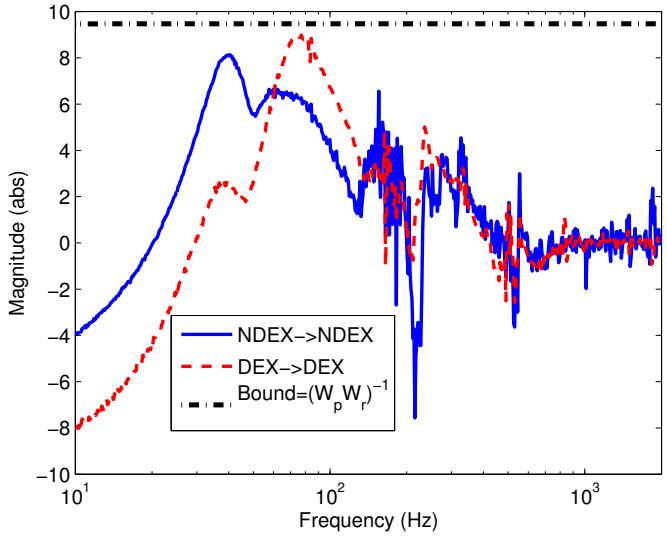

(b) 10,000 rpm

Figure 26: Bode plots of output sensitivity functions measured at various speeds.

[2] L. Barrett, "Stability and Nonlinear Response of Rotor-bearing Systems with Squeeze Film Bearings," Ph.D. dissertation, University of Virginia, 1979.

[3] J. Alford, "Protecting Turbomachinery From Self-Excited Rotor Whirl," *ASME J. Eng. for Power*, vol. 87, no. 4, pp. 333–344, October 1965.

[4] U. Schonhoff, "Practical Robust Control of Mechatronic Systems with Structural Flexibilities," Ph.D. Dissertation, Darmstadt Technical University, 2002.

[5] S. Skogestad and I. Postlethwaite, *Multivariable Feedback Control: Analysis and Design*. John Wiley & Sons, 2005.

[6] J. Doyle, "Analysis of feedback systems with structured uncertainty," *IEE Proc. Part D (Control Theory and Applications)*, vol. 129, pp. 242–250, 1982.

[7] R. Kumaresan and D. Tufts, "Estimating the parameters of exponentially damped sinusoids and pole-zero modeling in noise," *IEEE Trans. Acoust. Spch. Signal Proc.*, vol. 30, no. 6, pp. 833–840, 1982.

[8] S. Mushi, Z. Lin, and P. Allaire, "Design, construction and modeling of a flexible rotor active magnetic bearing Test Rig," in *Proc. ASME Turbo Expo.*, no. GT2010-23619, Glasgow, UK, 2010, pp. 443–452.

[9] Honeywell and Lockheed-Martin, "Application of multivariable control theory to aircraft control laws; Final Report : Multivariable control design guidelines," Wright Laboratory, US Airforce Materiel Command, Tech. Rep. WL-TR-96-3099, 1996.

[10] F. Losch, C. Gahler, and R. Herzog, "Mu-Synthesis controller design for a 3MW pump running in AMBs," in *Proc. 6th Int. Symp. Magn. Bearings*, 1998, pp. 415–428.

[11] R. Fittro and C. Knospe, "Rotor compliance minimization via mu-control of active magnetic bearings," *IEEE Trans. Contr. Syst. Technol.*, vol. 10, no. 2, pp. 238–249, 2002.

[12] F. Losch, "Identification and Automated Controller Design for Active Magnetic Bearing Systems," Ph.D. dissertation, ETH Zurich, 2002.

[13] M. Swann, "Ramping up magnetic bearing use," *Turbomachinery International*, vol. 50, no. 7, Novemer/December 2009.

[14] M. Franchek, "Selecting the Performance Weights for the μ and H∞ Synthesis Methods for SISO Regulating Systems," *ASME J. Dyn. Sys. Meas. Contr.*, vol. 118, pp. 126–131, 1996.

[15] E. Maslen and J. T. Sawicki, "Mu-Synthesis for magnetic bearings: Why use such a complicated tool?" in *Proc. ASME Int. Mech. Engr. Congr. Expo IMECE 2007*, no. 43033, 2007, pp. 1103–1112. [Online]. Available: http://link.aip.org/link/abstract/ASMECP/v2007/i43033/p1103/s1

[16] S. Garg, "Implementation Challenges for Multivariable Control: What You Did Not Learn in School!" NASA Glenn Research Center, Tech. Rep. NASA/TM-2008-215027, 2008.

[17] B. Ogunnaike, "A contemporary industrial perspective on process control theory and practice," *Ann. Rev. Control*, vol. 20, pp. 1–8, 1996. [Online]. Available: http://www.sciencedirect.com/science/article/B6V0H-43MCMVR-2/2/10194ba37549cf255efcacb4695e696c

[18] M. van de Wal, G. van Baars, F. Sperling, and O. Bosgra, "Multivariable H∞/μ feedback control design for high-precision wafer stage motion," *Control Engineering Practice*, vol. 10, pp. 739–755, 2002.

[19] R. Larsonneur, *Magnetic Bearings: Theory, Design, and Application to Rotating Machinery*. Springer, 2009, ch. 2: Principle of Active Magnetic Suspension, pp. 27–68.

[20] M. Englehart and M. Smith, "A four-block problem for H_∞ design: Properties and applications," in *Proc. 29th IEEE Conf. Decision Control*, vol. 4, 1990, pp. 2401–2406.

[21] M. Smith, "Well-Posedness of H$^\infty$ Optimal Control Problems," *SIAM J. of Control and Optim.*, vol. 28, no. 2, pp. 342–358, 1990.

[22] S. E. Mushi, "Robust Control of Rotordynamic Instability in Rotating Machinery Supported by Active Magnetic Bearings," Ph.D. dissertation, University of Virginia, Charlottesville, Virginia, 2012.

[23] S. Mushi, Z. Lin, and P. Allaire, "Robust control design for a supercritical rotor supported by AMBs," *IEEE Amer. Contr. Conf.*, 2012.

[24] G. Li, E. Maslen, and P. Allaire, "A note on ISO AMB stability margin," in *Proc. 10th Int. Symp. Magn. Brgs. ISMB10*, 2006, pp. 124–129.

[25] R. Williams, F. Keith, and P. Allaire, "Digital control of active magnetic bearings," *IEEE Tras. Ind. Electron.*, vol. 37, no. 1, pp. 19–27, 1990.

[26] R. Larsonneur, *Magnetic Bearings: Theory, Design, and Application to Rotating Machinery*. Springer, 2009, ch. 8: Control of the Rigid Rotor in AMBs, pp. 181–228.

[27] C. Cloud, E. Maslen, and L. Barrett, "Damping ratio estimation techniques for rotordynamic stability measurments," *ASME J. Eng. Gas Turb. Power*, vol. 131, 2009.

[28] M. Boerlage, "Rejection of disturbances in multivariable motion systems," Ph.D. Dissertation, Eindhoven University of Tehnology, 2008.

Appendix A
State Space Description

A complete state-space description for the uncertain plant with including the dynamic contribution of performance weighting functions and the modeled uncertainty from the bending modes is

$$P(s) := \left\{ \begin{bmatrix} \dot{x}(t) \\ c(t) \\ z(t) \\ y(t) \end{bmatrix} = \begin{bmatrix} A & B_\Delta & B_1 & B_2 \\ C_\Delta & 0 & 0 & 0 \\ C_1 & 0 & D_{11} & D_{12} \\ C_2 & 0 & 0 & 0 \end{bmatrix} \begin{bmatrix} x(t) \\ v(t) \\ w(t) \\ u(t) \end{bmatrix}, \quad v(t) = \Delta c(t) \right. \tag{11}$$

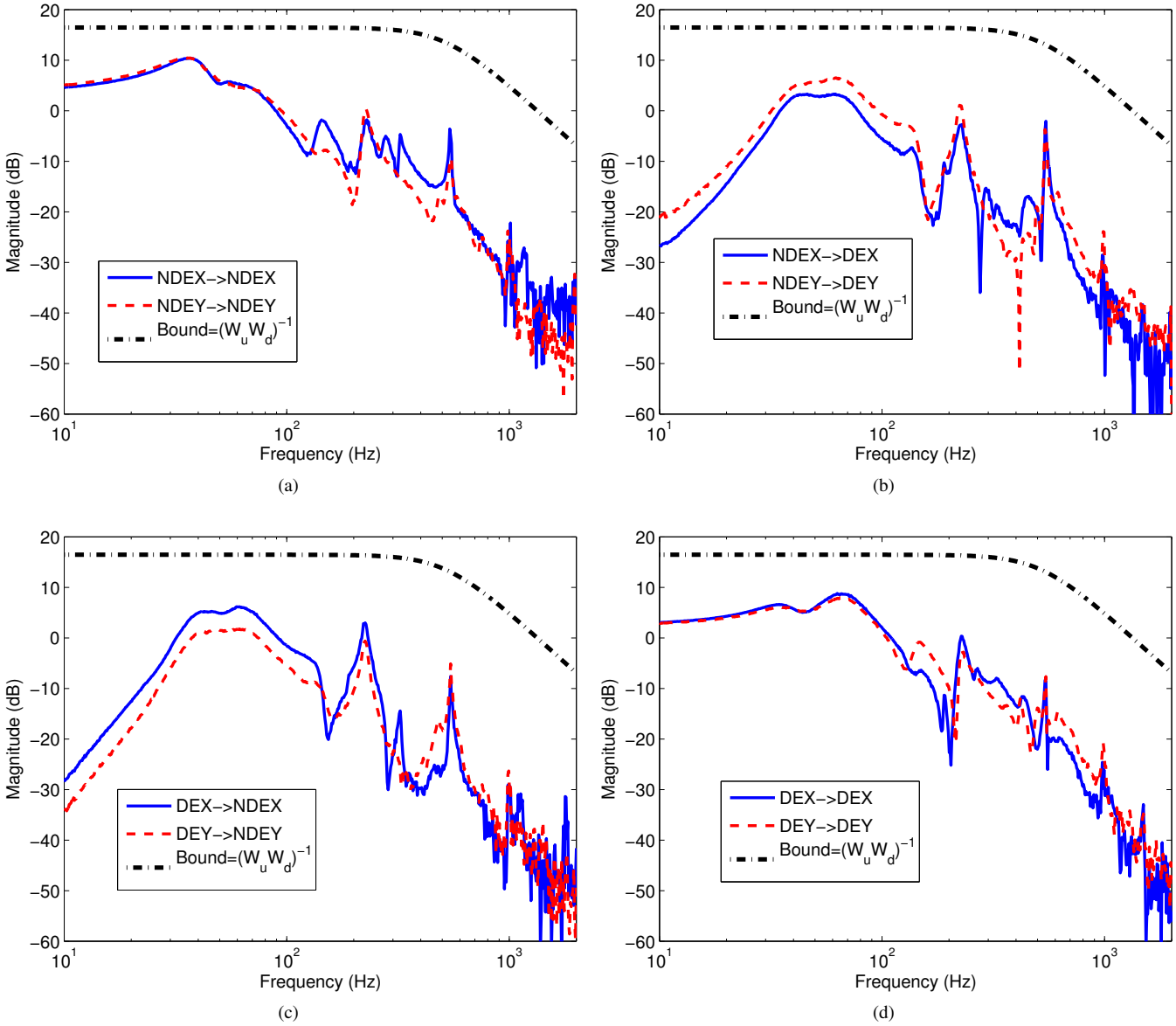

Figure 27: Bode plots of measured complementary sensitivity function or closed-loop response.

where

$$
\begin{aligned}
A &= \begin{bmatrix} \hat{A}_r & 0 & 0 & 0 \\ B_{d,u}C_{r,s} & A_d & 0 & 0 \\ -B_{w,p}D_dC_{r,s} & -B_{w,p}C_d & A_{w,p} & 0 \\ 0 & 0 & 0 & A_{w,u} \end{bmatrix} \\
B_\Delta &= \begin{bmatrix} 0 & I_2 & 0 & I_2 & 0 \end{bmatrix}^\top \\
c_\Delta &= \begin{bmatrix} 0 & -2\omega_3^2 & 0 & -2\zeta\omega_3 & 0 \\ 0 & -2\omega_4^2 & 0 & -2\zeta\omega_4 & 0 \end{bmatrix} \\
C_\Delta &= \begin{bmatrix} c_\Delta & c_\Delta \end{bmatrix}
\end{aligned}
$$

$$
\begin{aligned}
B_1 &= \begin{bmatrix} \hat{B}_r W_d & 0 & 0 & 0 \\ 0 & 0 & B_{w,p}W_r & 0 \end{bmatrix}^\top \\
B_2 &= \begin{bmatrix} \hat{B}_r & 0 & 0 & B_{w,u} \end{bmatrix}^\mathrm{T} \\
C_1 &= \begin{bmatrix} -D_{w,p}D_dC_{r,s} & -D_{w,p}C_d & C_{w,p} & 0 \\ 0 & 0 & 0 & C_{w,u} \end{bmatrix} \\
C_2 &= \begin{bmatrix} D_dC_{r,s} & C_d & 0 & 0 \end{bmatrix} \\
D_{11} &= \begin{bmatrix} 0 & W_rD_{w,p} \\ 0 & 0 \end{bmatrix} \\
D_{12} &= \begin{bmatrix} 0 \\ D_{w,u} \end{bmatrix}
\end{aligned}
\tag{12}
$$

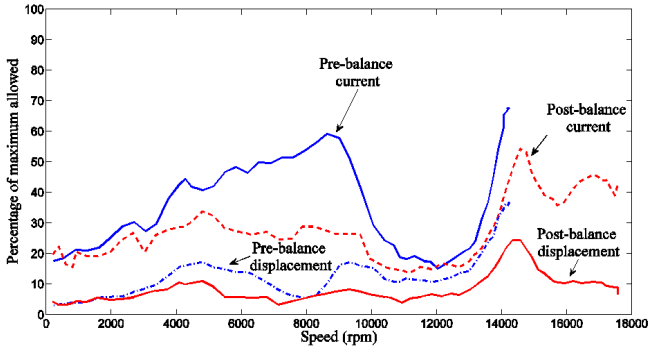

Figure 28: Rotor displacement (0-pk) and perturbation current at the NDE AMB as a percentage of the minimum clearance and bias current, respectively during a run-up to 18,000 rpm. Measurements are taken both before and after dynamic balancing.

and where ω_3 and ω_4 are the nominal natural frequencies of the first two bending modes Nc3 and Nc4, and $\zeta = 0.2\%$ is the modal damping. The uncertain state space model P contains 48 states, a contribution of 36 states from rotor-AMB model G, and 12 states from the dynamics of $W_p(s)$ and $W_u(s)$ repeated across four control channels. Balancing using a diagonal similarity transformation was used to improve the numerical conditioning of state-space representation of P.

Appendix B
Nondiagonal Performance Weights

Nondiagonal performance weights show promise as means of maximally exploiting the available degrees of freedom during control synthesis [28]. The MBTRI plant in the presence of significant cross-coupling the plant becomes less diagonally dominant. This suggests that a controller synthesized with nondiagonal weighting functions may have additional degrees of freedom to optimize the overall closed-loop sensitivity leading to performance improvements. Four prototype nondiagonal scalings were developed to systematically evaluate the effects of coupling and directionality between multiple control channels:

1) Full block performance weight

$$W_{p,1}(s) = \begin{bmatrix} 1 & 1 & 1 & 1 \\ 1 & 1 & 1 & 1 \\ 1 & 1 & 1 & 1 \\ 1 & 1 & 1 & 1 \end{bmatrix} \times \text{blkdiag}\left[W_{p,NDE}, W_{p,DE}, W_{p,NDE}, W_{p,DE}\right] \quad (13)$$

2. Cross-coupled performance weight

$$W_{p,2}(s) = \begin{bmatrix} 1 & 0 & 0.5 & 0 \\ 0 & 1 & 0 & 0.5 \\ 0.5 & 0 & 1 & 0 \\ 0 & 0.5 & 0 & 1 \end{bmatrix} \times \text{blkdiag}\left[W_{p,NDE}, W_{p,DE}, W_{p,NDE}, W_{p,DE}\right], \quad (14)$$

3. Simple block-diagonal

$$W_{p,3}(s) = \begin{bmatrix} 1 & 1 & 0 & 0 \\ 1 & 1 & 0 & 0 \\ 0 & 0 & 1 & 1 \\ 0 & 0 & 1 & 1 \end{bmatrix} \times \text{blkdiag}\left[W_{p,NDE}, W_{p,DE}, W_{p,NDE}, W_{p,DE}\right], \quad (15)$$

4. Block-diagonal with scaled off-diagonal terms

$$W_{p,4}(s) = \begin{bmatrix} 1 & 0.5 & 0 & 0 \\ 0.5 & 1 & 0 & 0 \\ 0 & 0 & 1 & 0.5 \\ 0 & 0 & 0.5 & 1 \end{bmatrix} \times \text{blkdiag}\left[W_{p,NDE}, W_{p,DE}, W_{p,NDE}, W_{p,DE}\right], \quad (16)$$

5. Block-diagonal with negative scaled off-diagonal terms

$$W_{p,5}(s) = \begin{bmatrix} 1 & -0.5 & 0 & 0 \\ -0.5 & 1 & 0 & 0 \\ 0 & 0 & 1 & -0.5 \\ 0 & 0 & -0.5 & 1 \end{bmatrix} \times \text{blkdiag}\left[W_{p,NDE}, W_{p,DE}, W_{p,NDE}, W_{p,DE}\right]. \quad (17)$$

The five controllers synthesized kept the same parameters for W_u, W_d and W_r as the benchmark case.

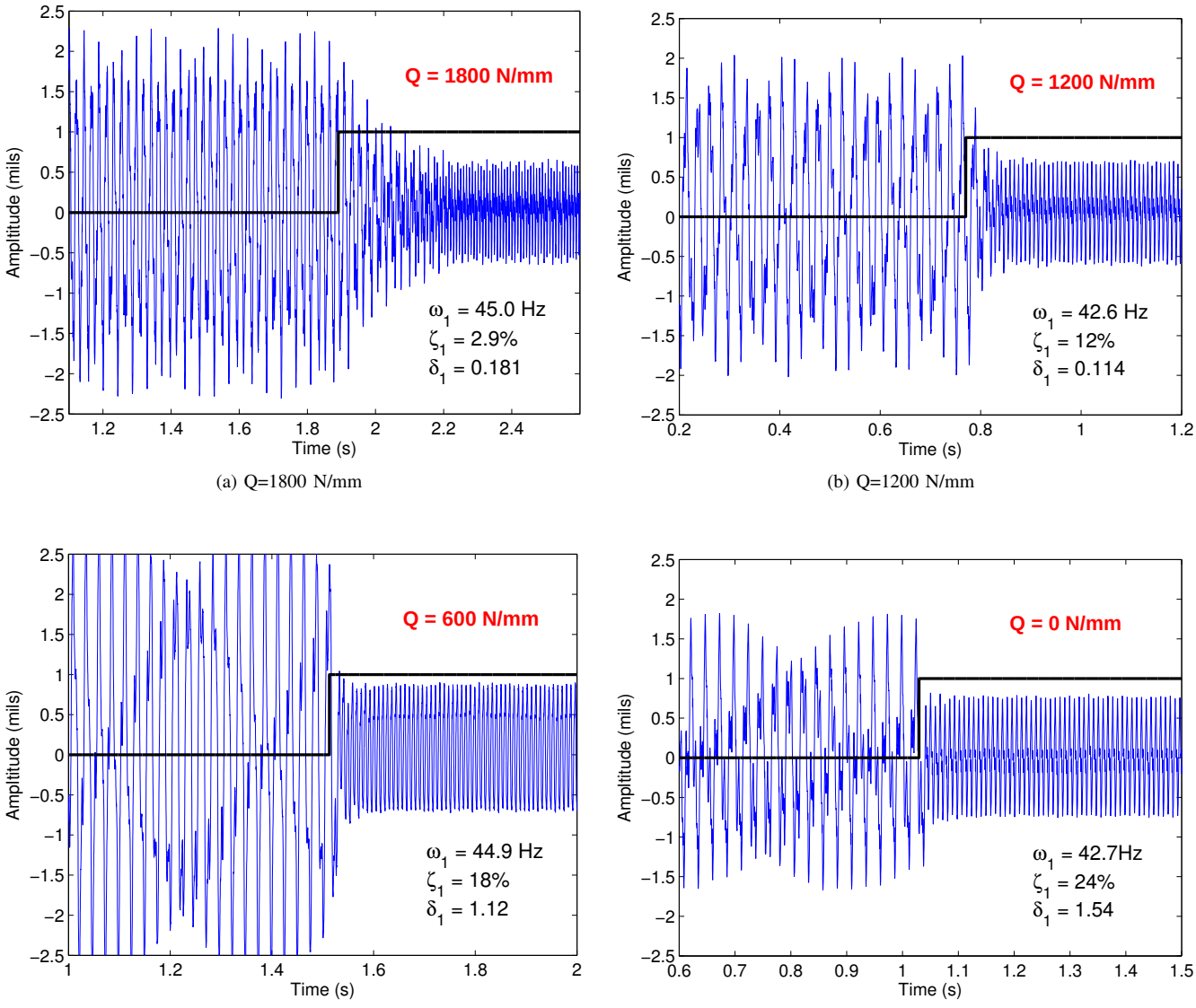

(a) Q=1800 N/mm

(b) Q=1200 N/mm

(c) Q=600 N/mm

(d) Q=0 N/mm

Figure 29: Rotor displacement response at 7,000 rpm on termination of blocking (indicated by the rising edge trigger) under different magnitudes of CCS excitation. Benchmark I controller is used to suspend the rotor and the stability threshold for this controller is 2000 N/mm.

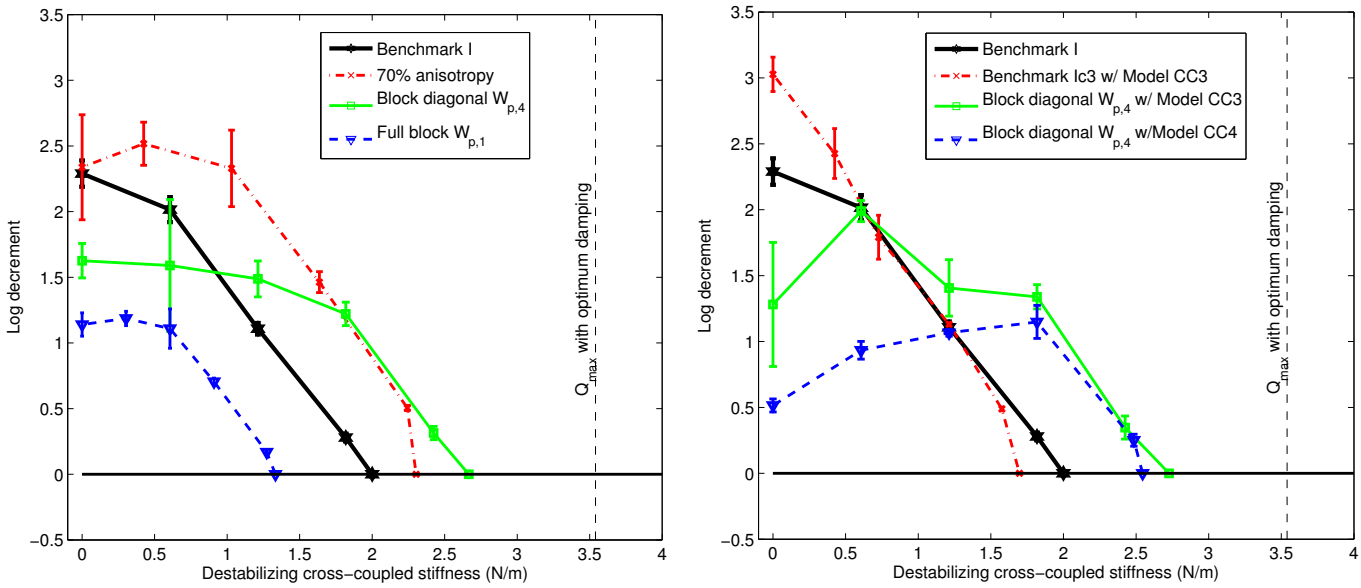

(a) Without CCS uncertainty model.

(b) With CCS uncertainty model.

Figure 30: Experimental stability sensitivity plot of log decrement of Nc1 versus destabilizing cross-coupled stiffness Q for several controllers compared with the Benchmark I.